Supplemental Materials for:

Ion Implantation of Magnesium Guests into Type II Silicon Clathrate Films, an Alternate Approach to Doping a Cage-like Silicon Allotrope

Joseph P. Briggs[1], Sam Saiter[2], Michael Walker[2], Shei S. Su[3], Michael Titze[3], Yongqiang Wang[4], Yinan Liu[1], Reuben T. Collins[2], Meenakshi Singh[2], Carolyn A. Koh[1]
1 *Department of Chemical and Biological Engineering, Colorado School of Mines, Golden, Colorado 80401, USA*
2 *Department of Physics, Colorado School of Mines, Golden, Colorado 80401, USA*
3 *Sandia National Laboratories, Albuquerque, New Mexico, 87123 USA and*
3 *Los Alamos National Laboratory, Los Alamos, New Mexico, 87545 USA*
(Dated: October 15, 2025)

IMPLANT PREPARATION

The synthesized low Na (x << 1) Na_xSi_{136} type II clathrate films underwent multiple characterization tests before focused ion beam (FIB) implantation gas detailed in the main text (e.g. XRD, Raman, SEM.) After samples were fully characterized optimal films were chosen for implantation, like the one shown in Fig. S1.a. A 50 μm (thick) steel shadow mask was used to deposit grid lines in a 13.5 mm square grid with each region being 2.4 mm wide. The grid lines consisted of a 3 nm Cr adhesion layer followed by a 15 nm Au layer deposited by RF sputtering. This mask, shown in Fig. S1.b, allowed for identification of different implant regions to test multiple micro implantation parameters. The different regions were indicated by a dot system also deposited onto the film surface to identify position under magnification. After this an implant plan based on capabilities of equipment was put together shown in Fig. S1.c indicating implant species, energy, size, fluence, and current. The Mg implant regions were 150 μm^2, shown in green, with implanter write zones of 200 μm^2, shown as the outline around the green square. For Li the implant write zones were also 200 μm^2 with 100 μm^2 implant regions for 1×10^{13} $/cm^2$ and 1×10^{14} $/cm^2$ and 25 μm^2 for 1×10^{15} $/cm^2$ fluence implants. Crosses were etched into the surface at some grid line intersections to help in identification as the mask could be difficult to see in the implanter camera, shown as the dark markings between

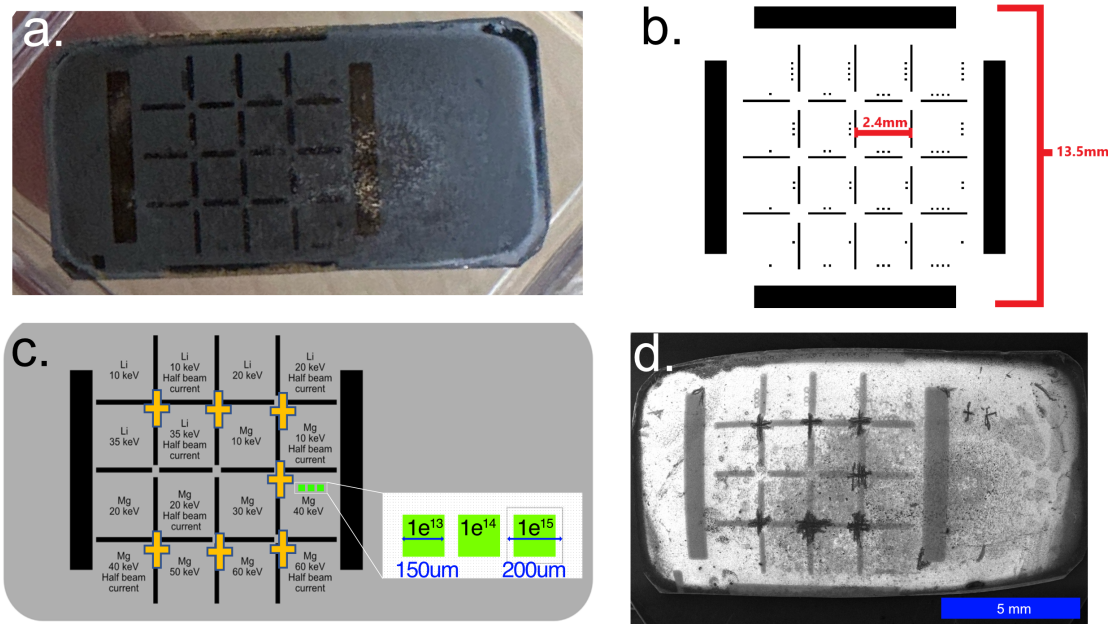

FIG. S1. a) Picture of a low Na (x << 1) Na_xSi_{136} type II clathrate film grown on Si substrate. b) Shadow mast pattern. c) Summary of implant regions indicating implant species, energy, and current. The green squares indicate dosages used in each implant region. The yellow crosses denote the crosses added to help identify implant areas in implanter camera and used in coordinate system. d) 15× magnified SEM image of the implanted Na_xSi_{136} type II clathrate film.

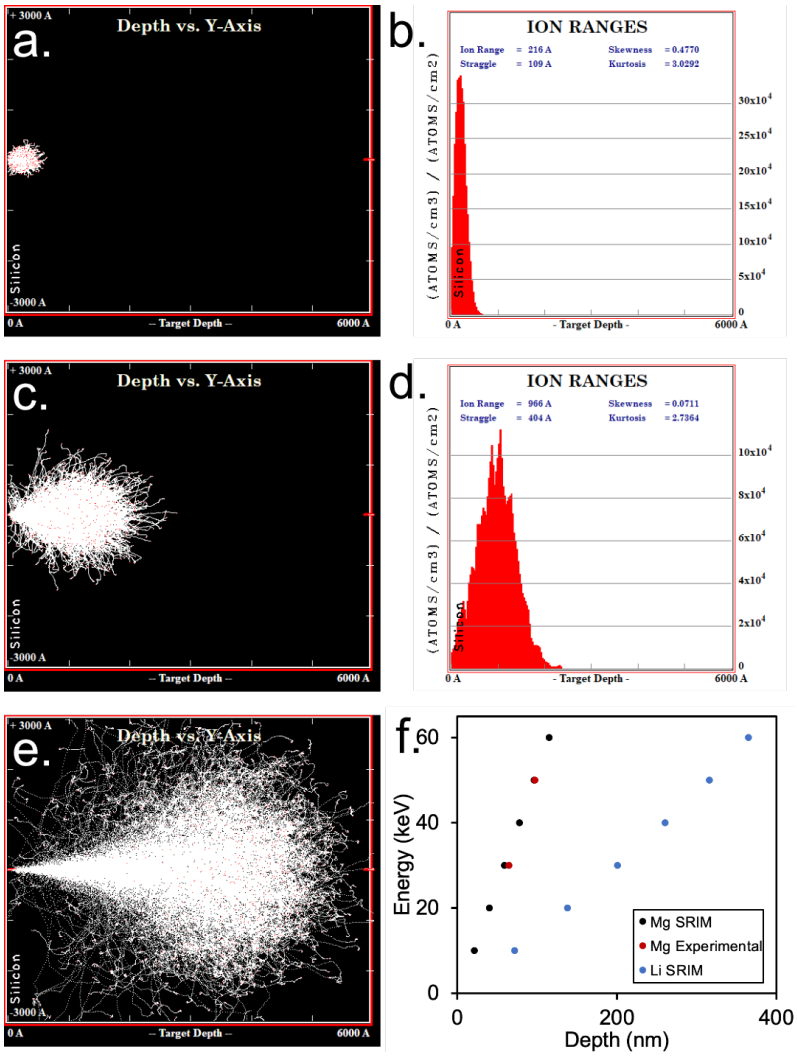

FIG. S2. SRIM calculations of implants into d-Si. Diamond Si was used as a similar approximate material since no Na_xSi_{136} type II clathrate film data exists as this is the first implantation study in these films. a) Implant profile of 10 keV Mg implant in d-Si. b) Ion range for 10 keV Mg implant. c) Implant profile of 60 keV Mg implant in d-Si. d) Ion range for 60 keV Mg implant. e) Implant profile of 60 keV Li implant in d-Si. f) Plot of the implant depth vs implant energy for both Li and Mg based on SRIM calculations in d-Si.

gridlines in the SEM image in Fig. S1.d.

Before implantation Stopping and Range of Ions in Matter (SRIM) calculations were performed using the SRIM online toolbox.[1] Since no Si clathrate data exists, diamond Si (d-Si) was used as a proxy due to similarity. However, we expect difference in implant ranges and straggle since the clathrate lattice is an open framework and less dense than d-Si however for approximation this was chosen as suitable. Implant profiles were calculated for both Mg and Li as shown in Fig. S2. As expected Li, which is lighter, implants would systematically deeper at each energy and has more straggle than Mg due to ion mass. These calculations were compared to TOF-SIMS results presented in the main text and helped inform interpretation of the results. Implant depth for two of the broad beam (BB) implants performed under the same conditions are shown in red in S2.f.

TABLE S1. Summary of tests implant species and implant parameters.

Implant	Type of implant	Fluence (cm^{-2})	Size	Energy	Current
Li	FIB	$1e^{13}$, $1e^{14}$, $1e^{15}$	100 μm^2, 100 μm^2, 25 μm^2	10 keV	0.24 pA
Li	FIB	$1e^{13}$, $1e^{14}$, $1e^{15}$	100 μm^2, 100 μm^2, 25 μm^2	20 keV	0.44 pA
Li	FIB	$1e^{13}$, $1e^{14}$, $1e^{15}$	100 μm^2, 100 μm^2, 25 μm^2	35 keV	1.06 and 0.37 pA
Mg	FIB	$1e^{13}$, $1e^{14}$, $1e^{15}$	150 μm^2, 150 μm^2, 150 μm^2	10 keV	101.91 and 28.79 pA
Mg	FIB	$1e^{13}$, $1e^{14}$, $1e^{15}$	150 μm^2, 150 μm^2, 150 μm^2	20 keV	121.28 and 32.67 pA
Mg	FIB and BB	$1e^{13}$, $1e^{14}$, $1e^{15}$ $1e^{14}$, $1e^{15}$	150 μm^2, 150 μm^2, 150 μm^2 5 mm^2, 5 mm^2	30 keV	165.15 pA
Mg	FIB	$1e^{13}$, $1e^{14}$, $1e^{15}$	150 μm^2, 150 μm^2, 150 μm^2	40 keV	90.62 and 49.22 pA
Mg	FIB and BB	$1e^{13}$, $1e^{14}$, $1e^{15}$ $1e^{15}$, $7e^{15}$	150 μm^2, 150 μm^2, 150 μm^2 5 mm^2, 5 mm^2	50 keV	165.50 pA
Mg	FIB	$1e^{13}$, $1e^{14}$, $1e^{15}$	150 μm^2, 150 μm^2, 150 μm^2	60 keV	120.90 and 43.00 pA

Table S1 details out the parameters of each of the implantation experiments performed into the Na_xSi_{136} type II clathrate films. The implant species, type of implant either FIB or BB, fluence, implant area, energy, and currents used are each indicated.

ADDITIONAL IMPLANT CHARACTERIZATION

Calibration of the TOF-SIMS sputter time to the depth profile was necessary to determine the implant depths in Fig. 5 and 6. The TOF-SIMS sputter crater shown in the inset of Fig. S3.b was repeatedly measured in a stylus profiometer. A representative profile of a TOF-SIMS sputter crater created from measuring an Mg implant in a Na_xSi_{136} type II clathrate film is shown in Fig. S3.a. The irregular peaks at zero depth reflect surface roughness and structural inhomogeneities such as grain boundaries. However, the TOF-SIMS sputter crater can be easily identified

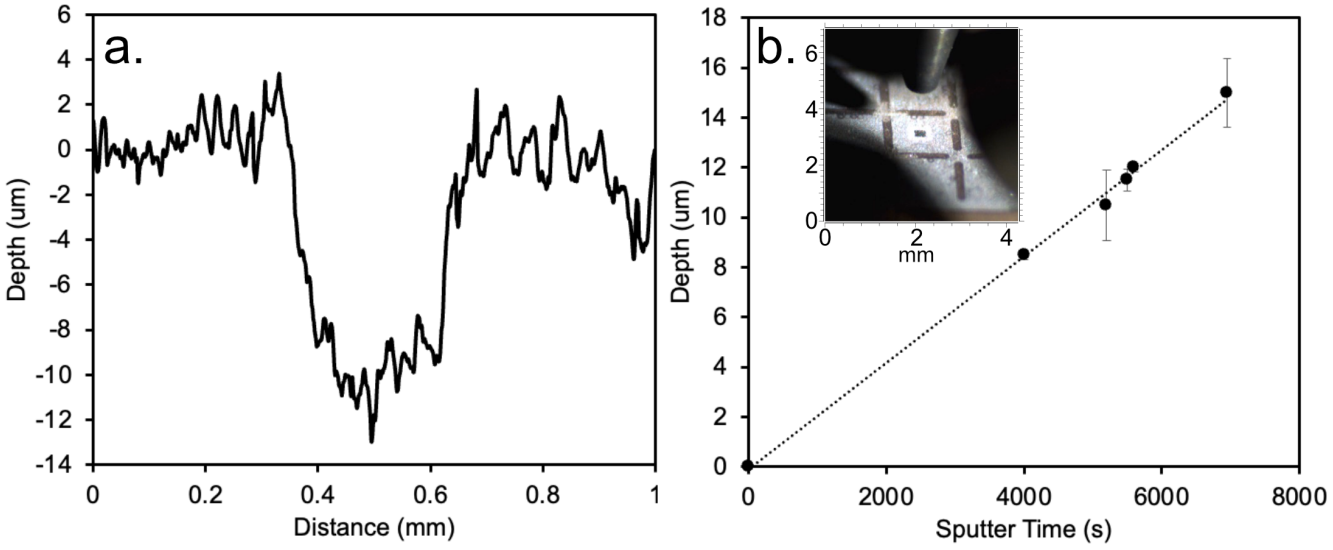

FIG. S3. a) Profilometer scan of Na_xSi_{136} type II Si clathrate after TOF-SIMS. The scan was taken across 1 mm and the sputter width was 300 μm. b) Sputter depth calculated from multiple profiles of sputter craters in the Si clathrate films at different sputter times. The inset indicating the sputter crater inside one of Mg implant regions inside the shadow mask of a Si clathrate film.

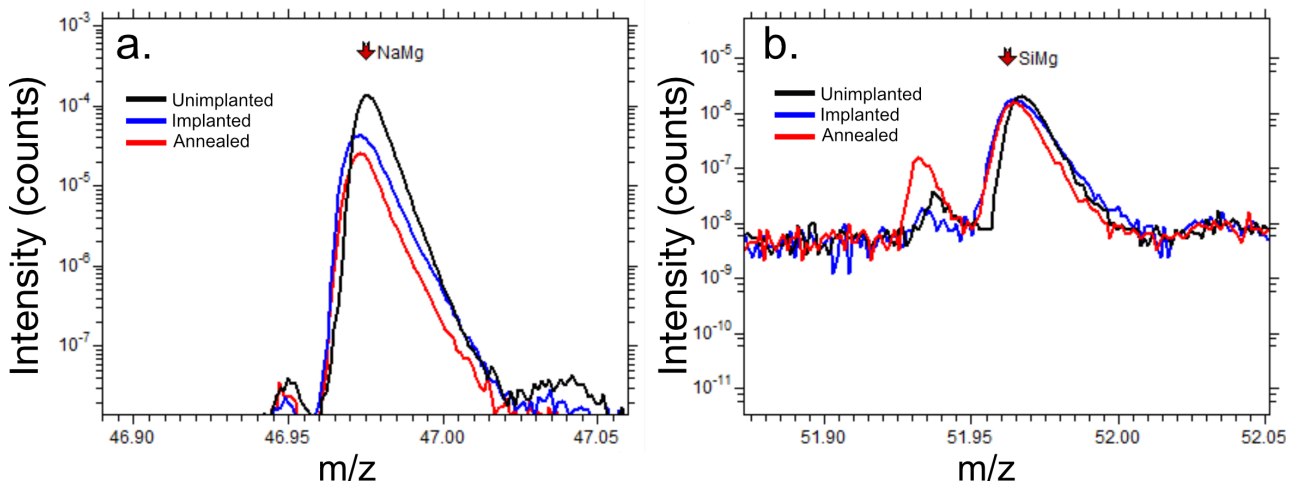

FIG. S4. a) TOF-SIMS plot of the peak around 47.00 m/z corresponding to the molecular weight of NaMg. b) TOF-SIMS plot of the peak around 52.00 m/z corresponding to the molecular weight of SiMg. The black curve is the unimplanted Na_xSi_{136} film. The blue is the film after implantation of 1×10^{15} $/cm^2$ fluence at 50 keV. The red is after an implant activation using a 12 sec ramp to 500°C, holding for 12 sec, and then removal from the RTA as described in the main text.

both visually and in the profile with the sharp dip to around $\sim$ 8 - 10 μm. An average of the sample surface height and TOF-SIMS sputter crater base was calculated and the difference was determined to be the sputter depth. This sputter depth can be compared to the TOF-SIMS sputter time as shown in Fig. S3.b to gain an idea of the implant depth in Fig. 5 and 6 in the main text. The error bars were determined by calculating the standard deviation in both sample height and sputter crater depth. The sputter depth increased linearly with sputter time.

Other species like NaMg and SiMg were looked for in the TOF-SIMS profiles to determine if any alloys or compounds were forming from the implant and activation process. While their presence is able to be detected as shown in Fig. S4 the counts, normalized to the TIY, were orders of magnitude below other species (Si, Na, Mg) and did not change significantly before or after implantation or activation. This indicates these are likely just impurities in the starting materials, samples, or detector background. While the electron paramagnetic resonance in Fig. 7 shows a decrease in the Na hyperfine lines of isolated Na electrons it does not appear these are forming a compound with Mg but could still be interacting with neighboring Mg. Mg-Mg pairs were also looked for in TOF-SIMS but due to mass overlap with over surface species, a defnitive signal was not able to be detected.

Large area Raman scans showed consistent amorphization of all BB implanted samples with 1×10^{15} $/cm^2$ fluence and above consistent with FIB samples. The 1×10^{14} $/cm^2$ fluence at 30 keV showed the type II Si clathrate structure remained intact after implantation and after annealing at 500°C for 12 s in the RTA. The higher fluence and higher energy implants 1×10^{15} $/cm^2$ at 50 keV showed amorphous before and after annealing. Interestingly the 1×10^{15} $/cm^2$ at 30 keV showed amorphous in Raman scans across the sample before annealing, but small, but noticeable, type II clathrate peaks emerged after annealing at multiple locations. This can be seen in the blue spectra in Fig. S5 with the peaks around 280 and 464 cm^{-1}. This indicates potential recovery of the clathrate structure.

To test the effects of the annealing process without implantation on the CW-EPR, a low Na Na_xSi_{136} film synthesized under the same parameters was measured. The film was SF_6 etched under the same parameters and showed no a-Si, d-Si, or type I defects in XRD. Fig S6.a shows the room temperature EPR spectrum before and after annealing for 12 sec at 500°C in the RTA. The film before annealing shows typical dangling bond and small free carrier features, which can vary between samples. After annealing the dangling bond feature decreased while the free carrier line increased significantly. This decrease in dangling bonds is consistent with what was observed with Raman in Fig S6, showing that after annealing some clathrate reappears at the damaged amorphous surface. The increase in free carriers is interesting and can be explained by the Na atoms redistributing into a more conductive state during the anneal.

The low temperature CW-EPR of the annealed sample in RTA shown in Fig S6.b is also interesting. The hyperfine lines, cluster Na feature, and free carrier line all increase while the dangling bond feature again decreases. This is inconsistent with the Mg implanted and annealed samples as these saw suppression of the hyperfine lines when the cluster feature increased. The dangling bond and free carrier features are close together with g value of 2.005 and 2.003 respectively. S6.c shows this region of the spectra to highlight the decrease in dangling bonds after annealing and increase of free carriers. The integrated intensity, shown in S6.d, increased about four fold after annealing indicating

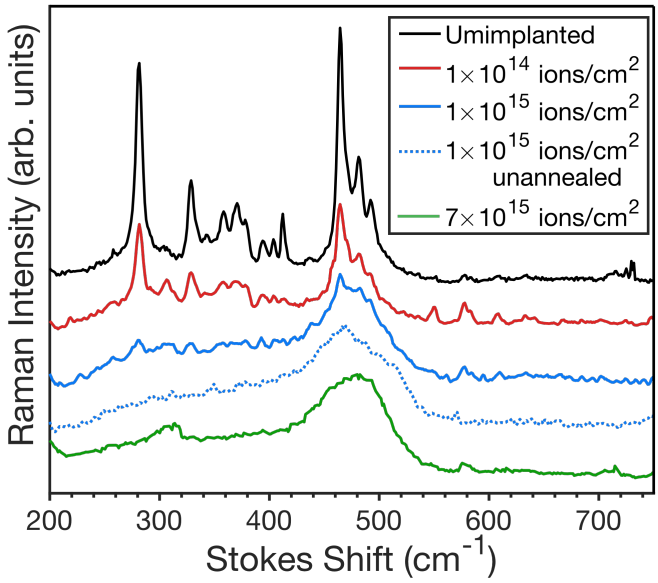

FIG. S5. Confocal Raman Spectroscopy spectra of an unannealed (black), and implanted and annealed samples with different Mg fluences 1×10^{14} $/cm^2$ (red), 1×10^{15} $/cm^2$ (blue with unannealed shown with the dashed spectra), and 7×10^{15} $/cm^2$ (green).

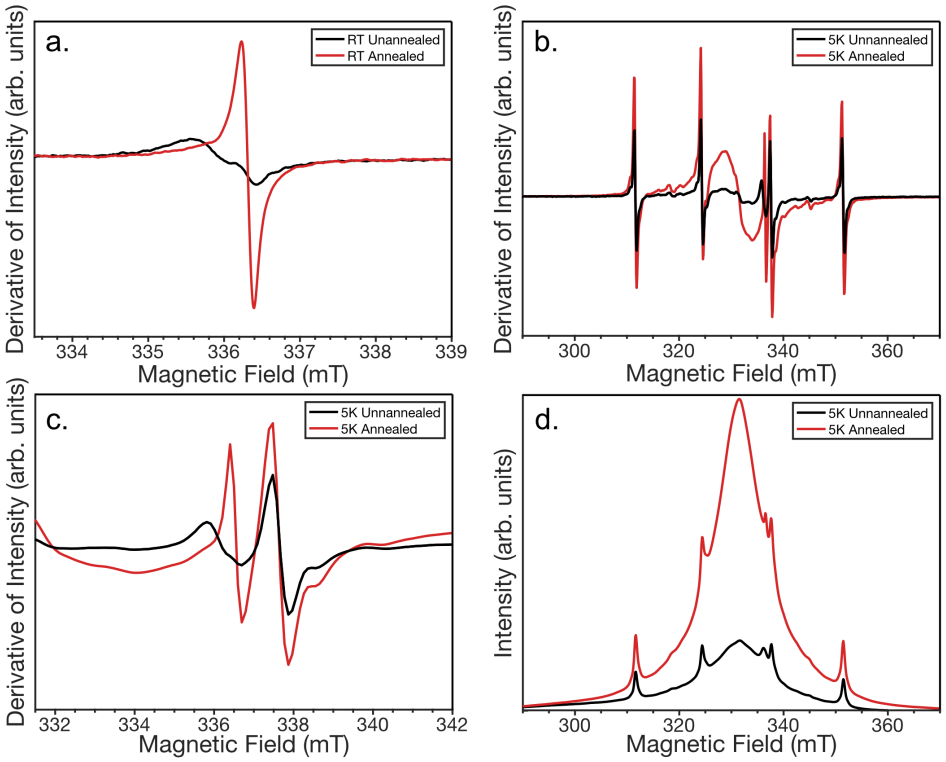

FIG. S6. a) Room and b) low (5 K) temperature CW-EPR spectra of a Na_xSi_{136} film before annealing for 12 s at 500°C in RTA (black) and after annealing (red). The spectra were acquired under the same parameters at 9.44 GHz over 10 scans at room temperature and 5 scans at low temperature and scaled by sample weight. c) The low temperature spectra over 10 mT centered around the dangling bond, free carrier, and third hyperfine line features. d) Integrated absorption spectra of the film before and after annealing.

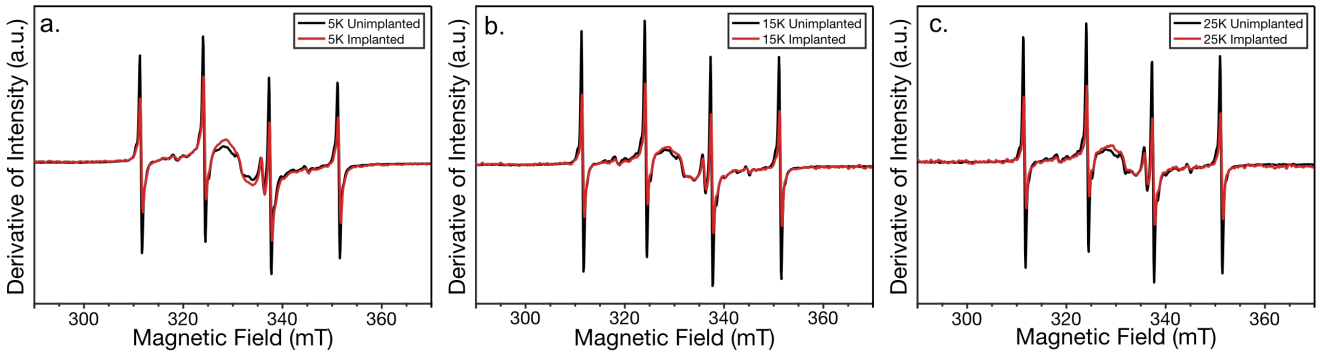

FIG. S7. Low temperature CW-EPR of Na_xSi_{136} film before implantation (black) and after implantation and activation (red). The spectra were acquired under the same parameters at 9.44 GHz over 40 scans at room temperature and 10 scans at low temperature and scaled by sample weight. a) 5K, b) 15 K, c) 25 K

much greater spin density. Since no implantation or introduction of new guests occurred these spins must be coming from somewhere else. It is possible the film has some Na dense regions which are largely spin inactive. During the anneal these could spread out into clusters or isolated Na indicating increases in these features and overall spin density. Alternatively, the defects in the sample could be interacting with Na electrons causing them to be spin inactive and as the defects are restored through the anneal these electrons could lead to some of the carrier concentration increase. The temperature dependence of the EPR is shown in Fig S7.

REFERENCES

[1] J. F. Ziegler, M. D. Ziegler, and J. P. Biersack, Nuclear Instruments and Methods in Physics Research Section B: Beam Interactions with Materials and Atoms **268**, 1818 (2010).